FSI Simulations of Pulse Wave Propagation in Human Abdominal Aortic Aneurysm: The Effects of Sac Geometry and Stiffness

Han Li, Kexin Lin and Danial Shahmirzadi

Department of Mechanical Engineering, Stevens Institute of Technology, Hoboken, NJ, USA.

ABSTRACT: This study aims to quantify the effects of geometry and stiffness of aneurysms on the pulse wave velocity (PWV) and propagation in fluid–solid interaction (FSI) simulations of arterial pulsatile flow. Spatiotemporal maps of both the wall displacement and fluid velocity were generated in order to obtain the pulse wave propagation through fluid and solid media, and to examine the interactions between the two waves. The results indicate that the presence of abdominal aortic aneurysm (AAA) sac and variations in the sac modulus affect the propagation of the pulse waves both qualitatively (eg, patterns of change of forward and reflective waves) and quantitatively (eg, decreasing of PWV within the sac and its increase beyond the sac as the sac stiffness increases). The sac region is particularly identified on the spatiotemporal maps with a region of disruption in the wave propagation with multiple short-traveling forward/reflected waves, which is caused by the change in boundary conditions within the saccular region. The change in sac stiffness, however, is more pronounced on the wall displacement spatiotemporal maps compared to those of fluid velocity. We conclude that the existence of the sac can be identified based on the solid and fluid pulse waves, while the sac properties can also be estimated. This study demonstrates the initial findings in numerical simulations of FSI dynamics during arterial pulsations that can be used as reference for experimental and in vivo studies. Future studies are needed to demonstrate the feasibility of the method in identifying very mild sacs, which cannot be detected from medical imaging, where the material property degradation exists under early disease initiation.

KEYWORDS: fluid–solid interaction (FSI), vascular biomechanics, pulse wave imaging (PWI), abdominal aortic aneurysm (AAA)

CITATION: Li et al. FSI Simulations of Pulse Wave Propagation in Human Abdominal Aortic Aneurysm: The Effects of Sac Geometry and Stiffness. *Biomedical Engineering and Computational Biology* 2016:7 25–36 doi:10.4137/BECB.S40094.

TYPE: Original Research

RECEIVED: May 4, 2016. **RESUBMITTED:** June 28, 2016. **ACCEPTED FOR PUBLICATION:** July 2, 2016.

ACADEMIC EDITOR: Kayvan Najarian, Editor in Chief

PEER REVIEW: Three peer reviewers contributed to the peer review report. Reviewers' reports totaled 453 words, excluding any confidential comments to the academic editor.

FUNDING: Authors disclose no external funding sources.

COMPETING INTERESTS: Authors disclose no potential conflicts of interest.

CORRESPONDENCE: dshahmir@stevens.edu

Paper subject to independent expert single-blind peer review. All editorial decisions made by independent academic editor. Upon submission manuscript was subject to anti-plagiarism scanning. Prior to publication all authors have given signed confirmation of agreement to article publication and compliance with all applicable ethical and legal requirements, including the accuracy of author and contributor information, disclosure of competing interests and funding sources, compliance with ethical requirements relating to human and animal study participants, and compliance with any copyright requirements of third parties. This journal is a member of the Committee on Publication Ethics (COPE).

Published by Libertas Academica. Learn more about this journal.

Introduction

Changes in the mechanical properties of the arterial wall have been shown to disrupt the normal hemodynamics of the arteries and contribute to various cardiovascular diseases (CVDs).[1] In particular, changes in aortic stiffness have been reported in prior studies as an independent indicator of all-cause and CVD-related mortalities.[2–5] Assessing the arterial stiffness has been collectively and increasingly recommended to be an essential part of clinical diagnosis, therapy, and follow-up procedures.[6,7] Abdominal aortic aneurysm (AAA) is one of the leading causes of cardiovascular-related morbidity and mortality in United States and worldwide, with an increasing prevalence in recent years.[8–10] The most common criterion currently used in assessing rupture risk and clinical intervention of AAAs is based on sac size (eg, when a sac diameter reaches ~5–5.5 cm or when the growth rate reaches 1 cm per year).[11–13] However, studies have shown that diameter alone may not be the most decisive factor in decision making, because some small AAAs could rupture while some large ones could survive during the normal life expectancy of the patient.[14–16] Therefore, such size-based intervention methods may offer insufficient or unnecessary treatments for different patients, and new criteria are needed for making reliable and effective interventions. On the other hand, it has been shown that the development of AAA constitutes alterations in the contents and fibrillar structures of elastin and collagen, which therefore induce local changes in the wall's mechanical properties.[9,17] In particular, degradation of the elastin content and structure has been associated with the local softening of the wall and balloon-like dilation, while collagen failure has been linked to sac failure.[16,18] Therefore, changes in the structural and mechanical properties of the wall are expected to take place at earlier stages of development than geometric changes that can be detected at later stages of the disease, and the use of biomarkers related to the wall's mechanical properties may improve disease diagnosis.

A set of techniques for the estimation of arterial stiffness is based on dilation–pressure curves;[19] but it has the major drawbacks of being invasive—eg, the use of pressure catheters—or incurring potentially large inaccuracies—eg, using non-patient-specific peripheral-to-central pressure transfer functions.[20,21] The second category of methods is based on the velocity of the pulsatile wave traveling along the aorta.

Pulse wave velocity (PWV) has been shown to be related to the underlying wall stiffness by the Moens–Korteweg formula.[22–24] The current clinical gold standard for PWV estimation is based on measuring the temporal pulse profiles at carotid and femoral arteries[6,25] and obtaining an average velocity as the distance measured over the skin divided by the time delay between the pulse profiles.[26,27] The carotid–femoral-based methods are prone to inaccuracies, being primarily induced by not using the exact arterial geometry, eg, the true traveled distance. In addition, assuming a single longitudinal flow direction between the carotid and the femoral arteries leads to further inaccuracies in measuring the true distance.[6,28] Moreover, the wall stiffness—and thus PWV—has been shown to vary regionally along the vascular branch,[19] and assuming an average PWV for the entire carotid-femoral segment might not thus represent a meaningful assessment. To overcome this problem, imaging techniques may be used as noninvasive alternatives for obtaining regional wall motions.[29–31] In particular, the ultrasound-based method of pulse wave imaging (PWI) has recently been developed by our group, aiming at obtaining the regional PWV noninvasively. PWI's feasibility studies have been performed on different applications such as normal and aneurysmal murine aortas[32,33] and human aortas in vivo,[30,34,35] human carotid in vivo,[36] aneurysmal and hypertensive patients,[37,38] canine aorta ex vivo,[39] experimental phantoms,[30,40] in fully coupled fluid–structure interaction (FSI) aortic simulations,[40–43] and in comparison with applanation tonometry.[30]

As indicated above, there occur local changes in AAA wall stiffness during disease progression, and therefore—based on a loose application of the Moens–Korteweg equation—the PWV is also expected to vary regionally. The performance of the PWI method can be compromised in applications involving sites of local changes in wall composition and geometry, such as arterial branching, aneurysms, and stenotic lesions, where precise detection of propagating waves becomes challenging due to the disruptive, complex patterns of the reflected waves.[33,44] Obtaining AAA samples at different stages of the disease with precisely controlled geometry and material properties in vivo is impossible. Therefore, simulation studies can be an efficient surrogate to simulate the pulsatile flow in healthy and AAA geometries with different sac wall geometry characteristics and stiffness values in order to gain insight into the effects of geometry and material properties on pulse wave propagation and velocity.

Conventional finite-element method (FEM) simulations of vascular biomechanics have primarily relied on solid-state (SS) modeling of blood vessels experiencing static or pulsatile internal pressure replicating the hemodynamic effects;[45] however, a more accurate description of fluid mechanics—as well as solid mechanics[46]—can be obtained by incorporating the two-way fluid–structure interaction (FSI) effects. Fully coupled FSI simulations using patient-specific geometries and anisotropic finite strain constitutive relations have been carried out for healthy and pathological arteries,[47–50] aiming at computing biomechanical properties such as fluid velocity and pressure as well as wall displacement and stress.[51,52]

FSI simulations using patient-specific AAA geometries have been previously performed to assess the risk of rupture by measuring the wall stress.[49,50,53–56] These studies have proposed that the wall stress reliably predicts potential rupture, as opposed to the traditionally used marker of AAA size. Fully dynamic FSI simulations can be used to quantify pulsatile wall radial displacement and its axial motion along the aorta over time and to calculate the PWV. There have been a few studies reporting temporal data on arterial radial wall displacement during dynamic FSI simulation but without recording the spatial data, and therefore no PWV measurements were made.[46] Even though the aortic tissues have been shown to behave under anisotropic, viscoelastic, nonlinear, and inhomogeneous regims,[10,16,47,50,53,57,58] the majority of arterial FSI simulation studies have been done on simplified material properties such as isotropic, elastic, linear, and homogenous scenarios. Previously, we had reported studies using coupled Eulerian–Lagrangian (CEL) FSI simulations of aortic pulse wave propagation, particularly on validating against phantom and in vitro canine studies[39,40] and on detecting wall local inclusions.[41,42]

In this study, CEL simulations of human aortas with straight as well as AAA geometries of different sac stiffness were performed to obtain the fluid-induced pulsatile wall deformations. The findings on the aortic pulsations can provide additional insight into pulse wave analysis in arteries with irregular geometry and wall properties and serve as the stepping stone for future studies on physiologically relevant geometrical and material parameters.

Materials and Methods

Modeling parameters. Human aortas with idealized normal (ie, non-aneurysmal) and AAA geometry were considered for modeling the arterial pulse wave propagation under cyclic fluid flow (Fig. 1). The AAA idealized geometry was generated based on the Eurostar standard dimensions using realistic preoperation measurements on 3,413 patients with infra-renal abdominal aortic aneurysms,[59] which was then used to generate the non-aneurysmal geometry by removing the sac. In order to reduce computational burden, a quarter of the entire axis-symmetric 3D model was used (Fig. 2). The CEL explicit solver in Abaqus 6.11-1 (Simulia) was used to perform the fully coupled FSI simulations in order to capture the mutual effects of the fluid and wall pulsatile wave motions on each other. The CEL solver has previously been validated in providing accurate description of the wave dynamics.[40,41] In CEL, the fluid dynamics is modeled with an Eulerian mesh domain, whereas the Lagrangian

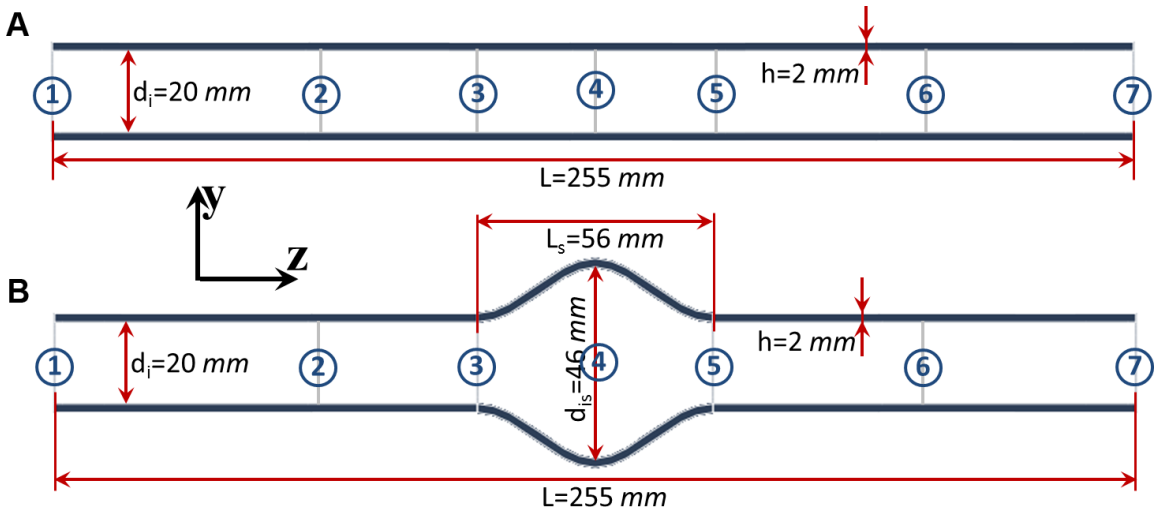

Figure 1. Schematics of idealized human aortic geometries: (**A**) straight, and (**B**) Eurostar AAA. Cross sections 1 and 7 indicate the boundary condition locations. On the AAA geometry, cross sections 3 and 5 define the sac zone, and cross sections 2 and 6 correspond to representative locations pre- and post-sac, respectively.

mesh domain is used to model the structural mechanics (see Appendix). According to the CEL solver requirement, the Eulerian domain was chosen to be large enough to ensure that it includes all Lagrangian elements at all times throughout the entire dynamic simulation. In order to match the ongoing counterpart experimental phantom studies, the fluid was modeled as water with material properties of density ρ = 1,000 kg/m^2, reference sound speed c_0 = 1,483 m/s, and dynamic viscosity μ = 1 mPa s. Similarly, the wall's material properties were defined to also mimic those from experimental phantom studies as were characterized under tensile and compressive mechanical testing within a strain range of ε = 0–10% at the rate of $\dot{\varepsilon}$ = 1%/s, using an Instron 5848 microtester and an ARES-G2 rheometer (TA Instrument), respectively. Given the rubber-like behavior of the phantom wall, the material behavior was defined as hyperelastic with the tensile–compressive experimental data to fit best to a third-order Ogden model using the Abaqus material assessment tool (Fig. 3) as follows:

$$W(\lambda_1,\lambda_2,\lambda_3)=\sum_{n=1}^{N}\frac{2\beta_n}{\alpha_n^2}(\lambda_1^{\alpha_n}+\lambda_2^{\alpha_n}+\lambda_3^{\alpha_n}-3);\quad (N=3) \quad (1)$$

where λ_i is the deviatoric principal stretches, and α_n and β_n are the material constants. A digital image correlation (DIC) system (Correlated Solutions Inc.) was used to measure the surface axial and lateral strain fields under uniaxial tension in order to estimate the Poisson's ratio (Fig. 3). Each axial and lateral strain was calculated as the average of the strain measurements at nine different local points on the specimen surface. The accuracy of DIC measurements was verified under zero strain field, eg, rigid body motion. The Lagrangian boundary conditions (BCs) were applied by fixing all six degrees of freedom (DOFs) on both ends of the

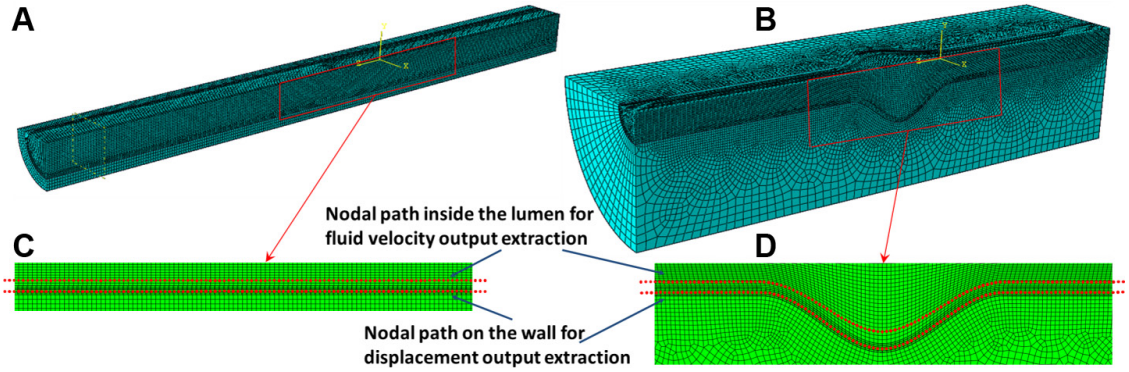

Figure 2. Quadrant 3D meshed geometries and the adjacent paths on the lower wall (Lagrangian nodes) and inside the lumen (Eulerian nodes) to be used for extraction of the wall displacement and fluid velocity outputs, respectively. (**A**, **C**) Straight and (**B**, **D**) Eurostar AAA geometries.

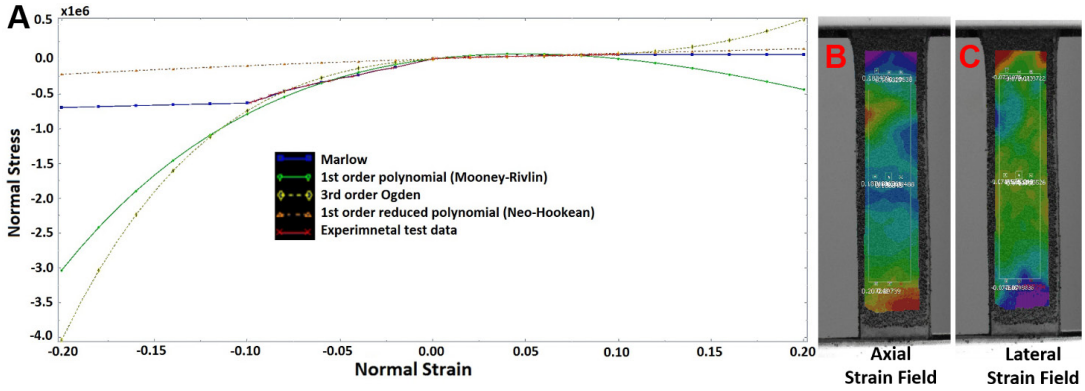

Figure 3. Mechanical testing of the phantom wall: (**A**) Experimental phantom stress–strain relationship along with the fits of different hyperelastic models. (**B**, **C**) DIC-obtained axial and lateral, respectively, strain maps that were used to obtain axial and lateral strains for Poisson's ratio calculation.

tube. On the Eulerian domain, a symmetrical BC was applied on the symmetry plane and a zero-pressure BC was applied on the tube outlet. Furthermore, fluid velocity with a sinusoidal profile with a magnitude of 3.63 m/s and a frequency of 5.4 Hz was also applied as the dynamic BC on the tube inlet to serve as the driving force for the fluid and the flow-induced solid motions. Similar to the material parameters, the flow parameters were chosen relevant to the pulsatile pump used in the ongoing experimental phantom studies.[39,40] Furthermore, two additional simulations were performed on AAA aortas with the same geometrical parameters, but the wall modulus at the sac zone (between sections 3 and 5 in Fig. 1) was set to be 1.5 times lower (softer sac) and 3 times higher (stiffer sac).[60–63] Assuming a similar hyperelastic regimen of the material behavior, the same experimental data obtained previously were mathematically scaled down/up to obtain pseudo-data for the softer/stiffer sacs, before similar third-order Ogden parametric model fit was performed on them.

Computational framework. A Precision T7600 workstation with Intel® Xeon® CPU (16 cores) at 3.10 GHz and 96 GB RAM was used to perform the computations. The mesh topology on the AAA quadrant axis-symmetric geometry contained a total of 233,520 elements, leading to a total computation time of 180 hours for a simulation time of 0.5 seconds (a time increment in the order of 1×10^7 seconds). A frame rate of 1,000 fps was used to extract the output parameters.

Output analysis. The radial component of the wall displacement, U_y, and the axial component of the fluid velocity, V_z, were extracted along the nodal paths on the lower wall (Lagrangian) and neighboring fluid inside the lumen (Eulerian), respectively (Fig. 2). The spatial data were plotted against time to obtain the spatiotemporal maps, allowing an easy and full visualization of the wave propagation and qualitative understanding of the local pulse wave propagation. Furthermore, the spatiotemporal maps were also used to calculate the PWV of the waves as the slope of the linear fit to the wave peaks in order to provide quantitative measures of the wave dynamics, as previously described in detail.[40–42]

Results

Material characteristics. The tensile–compressive stress–strain experimental data for the strain range of $\varepsilon = -10$–10% are shown in Figure 3A. Also shown in the figure are the strain–stress approximations based on the Marlow, Mooney, and Rivlin third-order Ogden and neo-Hookean hyperelastic models, being fitted within an extrapolated strain range of $\varepsilon = -20$–20%, in order to make sure that we were on the safe side of capturing possible large strains. The results showed the third-order Ogden model yielding the best fit of the experimental phantom stress–strain data while also describing the high-strain stiffening relevant to fibrillar soft biological tissues such as the aortic wall. The material parameters obtained from fitting to the experimental data, as well as to the scaled-down and scaled-up data (ie, softer and stiffer materials), are listed in Table 1. Figure 3B and C shows the DIC-based axial and lateral strain fields, respectively, for a representative specimen. Linear fitting to the average biaxial strain data resulted in a Poisson's ratio of $\nu = 0.49 \pm 0.06$ (n = 6), which is consistent with the nearly incompressible properties of soft tissues. A wall Poisson's ratio of $\nu = 0.49$ was used in the definition of the material properties.

Straight geometry with homogenous walls. The vertical component of wall displacement, U_y, and axial component

Table 1. Material constants of the third-order Ogden model for the soft, normal, and stiff walls obtained by Abaqus material behavior data-fitting module.

i		1	2	3
α_i	1.5 times softer	2.66	4.73	–1.46
	Normal	2.66	4.73	–1.46
	3 times stiffer	2.66	4.73	–1.46
β_i	1.5 times softer	–43259606.70	24844295.60	18814838.60
	Normal	–64889410.10	37266443.30	28222257.90
	3 times stiffer	–194668230.00	111799330.00	84666773.60

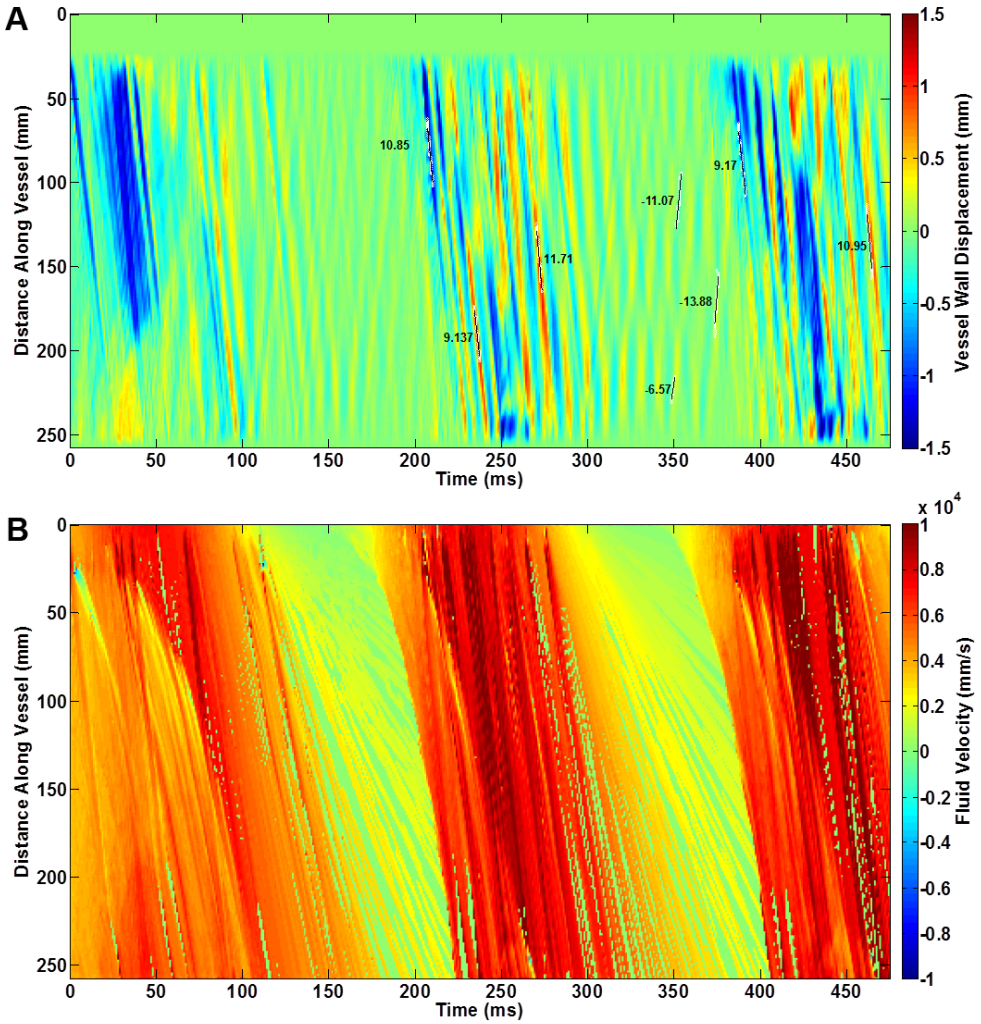

Figure 4. Spatiotemporal maps from the straight geometry aorta. (**A**) Vertical component of the wall displacement. (**B**) Axial component of the fluid velocity.

of the fluid velocity, V_z, were plotted in the spatiotemporal maps in Figure 4. There are three main cycles of the inlet pulsatile flow. Given the initial transient dynamics of the wave formation, only the second and third cycles were considered for obtaining the quantified results of the wave propagation throughout this study. The maps illustrate a relatively homogenous propagation of the wall and fluid pulse waves, with multiple pulse waves seen within each cycle. Between the cycles, there are primarily multiple weak reflected waves until the main forward wave comes in from the following cycle. Also shown in the figure is the regional PWVs estimated on the forward and reflected waves, showing relatively close PWVs on the forward (ie, positive velocity) and the reflected waves (ie, negative velocity).

AAA geometry with the softer sac. Figure 5 shows the spatiotemporal maps of the wall displacement vertical component, U_y, and fluid velocity axial component, V_z, obtained on the AAA geometry with the 1.5 times softer sac. Both the wall displacement and fluid velocity wave propagation indicate distinct patterns on the sac region, which is also marked on the maps based on an a priori known geometry. The wall displacement map (Fig. 5A) shows the sac to undergo higher displacement magnitudes with multiple forward and reflective waves that only travel within the sac zone boundaries. The homogenous propagation of the main forward wave is also seen to be disrupted at the sac region; however, it continues to propagate along the lumen after the sac. Also shown in Figure 5A is the regional PWV estimates on the forward and reflected waves, showing the pre-sac reflected waves to travel more slowly (eg, PWV = 5.8 ± 1.30 m/s) than the post-sac forward waves (eg, PWV = 9.39 ± 0.54 m/s). Short-traveling waves are also shown within the sac region traveling with the lowest velocities (eg, PWV = 4.55 ± 1.91 m/s).

AAA geometry with sac of the same stiffness. Figure 6 illustrates a frame of the fluid velocity magnitude vectors, V, on AAA geometry with the stiffness of the sac being the same as the stiffness of the rest of the aortic wall. The figure shows the propagation of a main forward-traveling fluid wave right after it has arrived at the sac. The entry of the fluid wave into the sac geometry is also accompanied by the creation of vortices, an observation that has also been reported by others.[51] Later on, a strongly attenuated chaotic motion was seen across

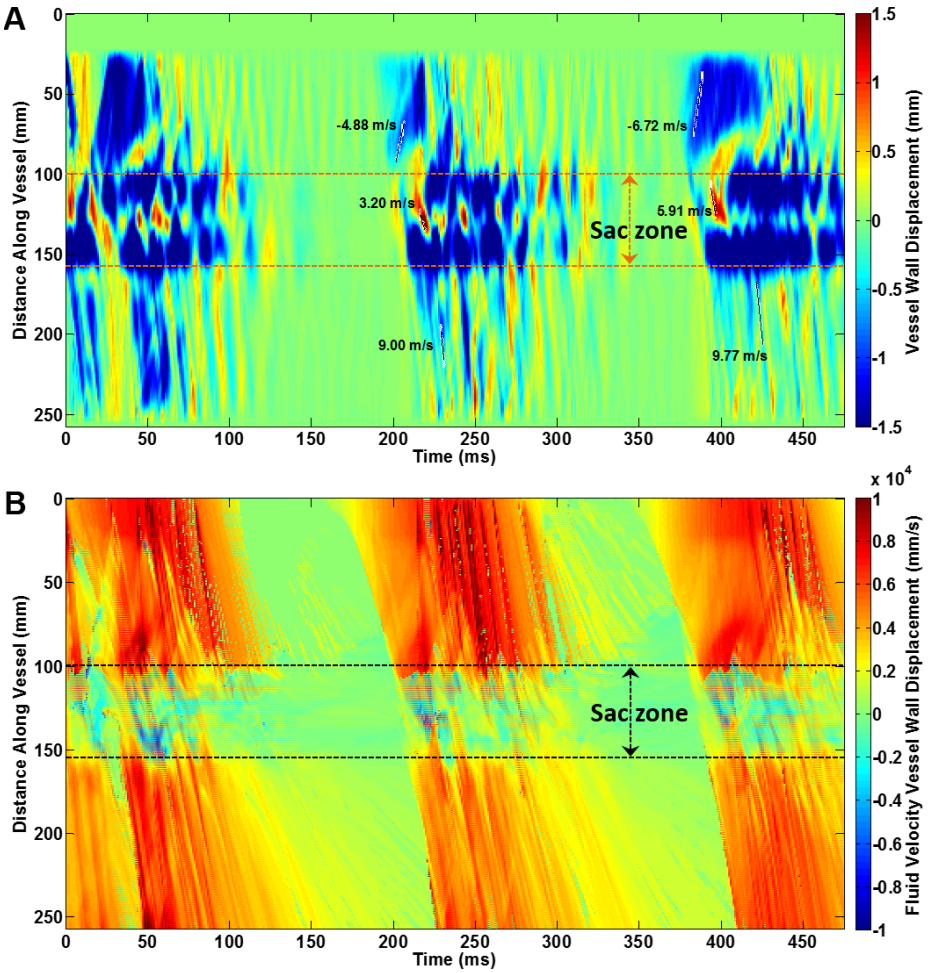

Figure 5. Spatiotemporal maps from the aneurysm geometry aorta with the sac walls 1.5 times softer than the rest of the walls of the aorta. (**A**) Vertical component of the wall displacement. (**B**) Axial component of the fluid velocity.

the wall, corresponding to a steadier and less turbulent flow past the peak of the inlet flow profile, until the next main forward wave comes in from the following pulse. The spatiotemporal maps of the wall displacement vertical component, U_y, and fluid velocity axial component, V_z, are shown in Figure 7. The general observation is similar to that of in Figure 5 for the soft sac model. In particular, the sac zone is clearly identifiable on both the wall displacement and fluid velocity spatiotemporal maps. Also shown on the figure are the regional PWV estimates on the forward and reflected

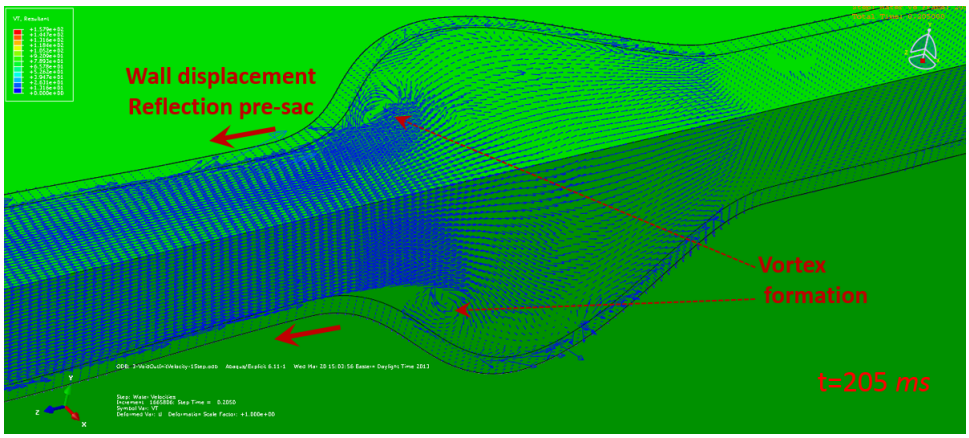

Figure 6. Vector representation of fluid velocity magnitude at the entrance of the sac at $t = 205$ ms. The formation of the vortex in the fluid corresponds to the formation of the reflected wave in the wall.

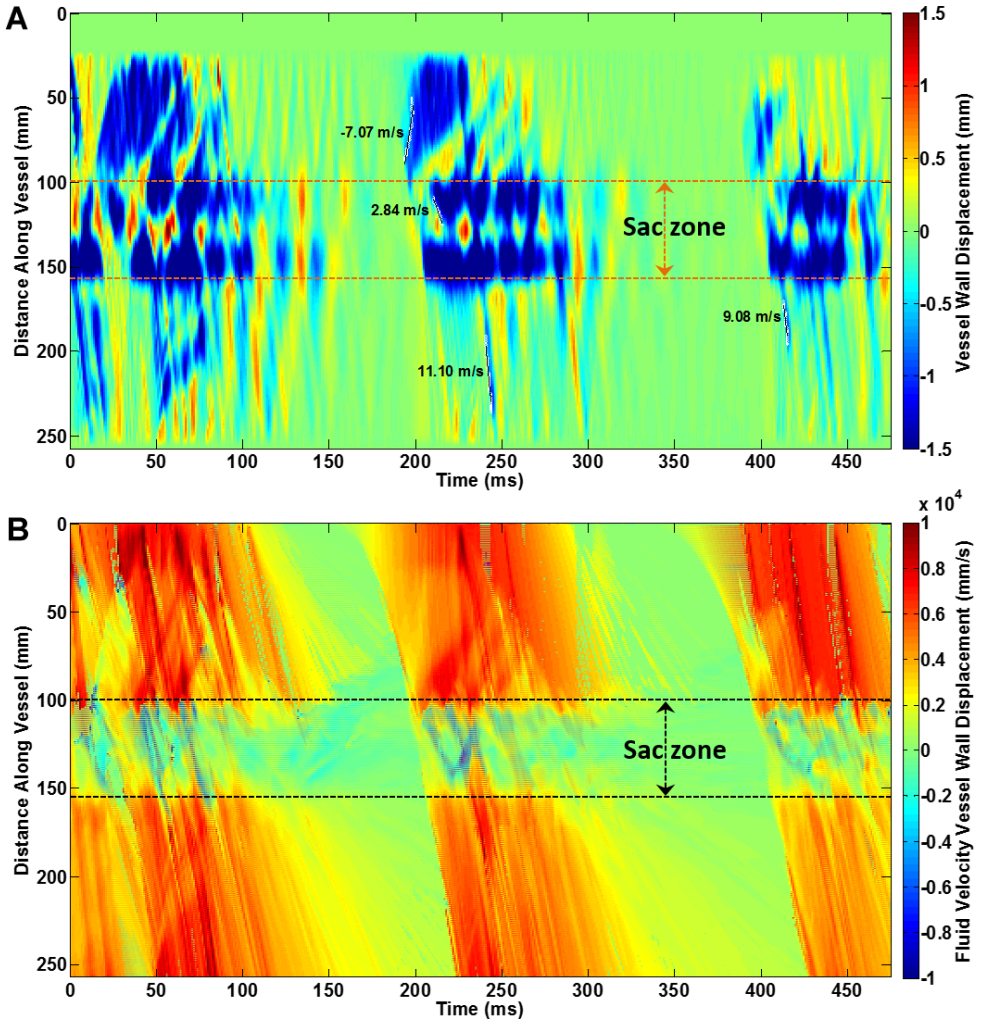

Figure 7. Spatiotemporal maps from the aneurysm geometry aorta with the sac walls possessing the same stiffness as the rest of the walls of the aorta. (**A**) Vertical component of the wall displacement. (**B**) Axial component of the fluid velocity.

waves. The results show that the pre-sac reflected waves travel more slowly (eg, PWV = 7.07 m/s) than the post-sac forward waves (eg, PWV = 10.09 ± 1.43 m/s). Yet, the short-traveling waves within the sac region show the slowest propagation (eg, PWV = 2.84 m/s).

AAA geometry with the stiffer sac. Figure 8 shows the spatiotemporal maps of the wall displacement vertical component, U_y, and the fluid velocity axial component, V_z, obtained on the AAA geometry with the 3 times stiffer sac. Compared to the two previous AAA models with softer sacs (Figs. 5 and 7), the results in Figure 8 show a lower displacement magnitude at the sac; however, the sac displacement is still higher than that of the rest of the wall. Compared to the previous softer sac models, the sac zone is not as distinguishable based on the wall displacement wave propagation, but the fluid velocity wave propagation still show the sac zone markedly. The pre-sac reflected and post-sac forward waves travel with PWVs of 4.52 ± 0.55 and 10.87 ± 0.69 m/s, respectively.

Wall displacement and fluid velocity temporal profiles. In order to obtain better insight into the fluid–solid interactions, Figure 9 illustrates the fluid velocity and wall displacement profiles at five different cross sections on the straight and AAA geometry aortas (see Fig. 1 for the cross-section locations). The results show that for the most part, the fluid velocity pulse is ahead of the wall displacement pulse for ~10–20 ms. As it goes further along the lumen, ie, increasing section number, the flow and displacement profiles get in more synchrony, which could possibly be explained by the fact that the flow—and thus the fluid–solid interaction—gets more developed as it propagates further along the vessel.

Discussion

FSI simulations can serve as a powerful and effective tool to study the arterial pulsatile motions. However, the results from the numerical methods should be interpreted within the limitations of such methods and under the full understanding of the underlying assumptions. In the present study, three full cycles of a pulsatile wave were simulated. However, in order to minimize the transient dynamics in the wave development and propagation, quantitative analyses such as PWV estimates

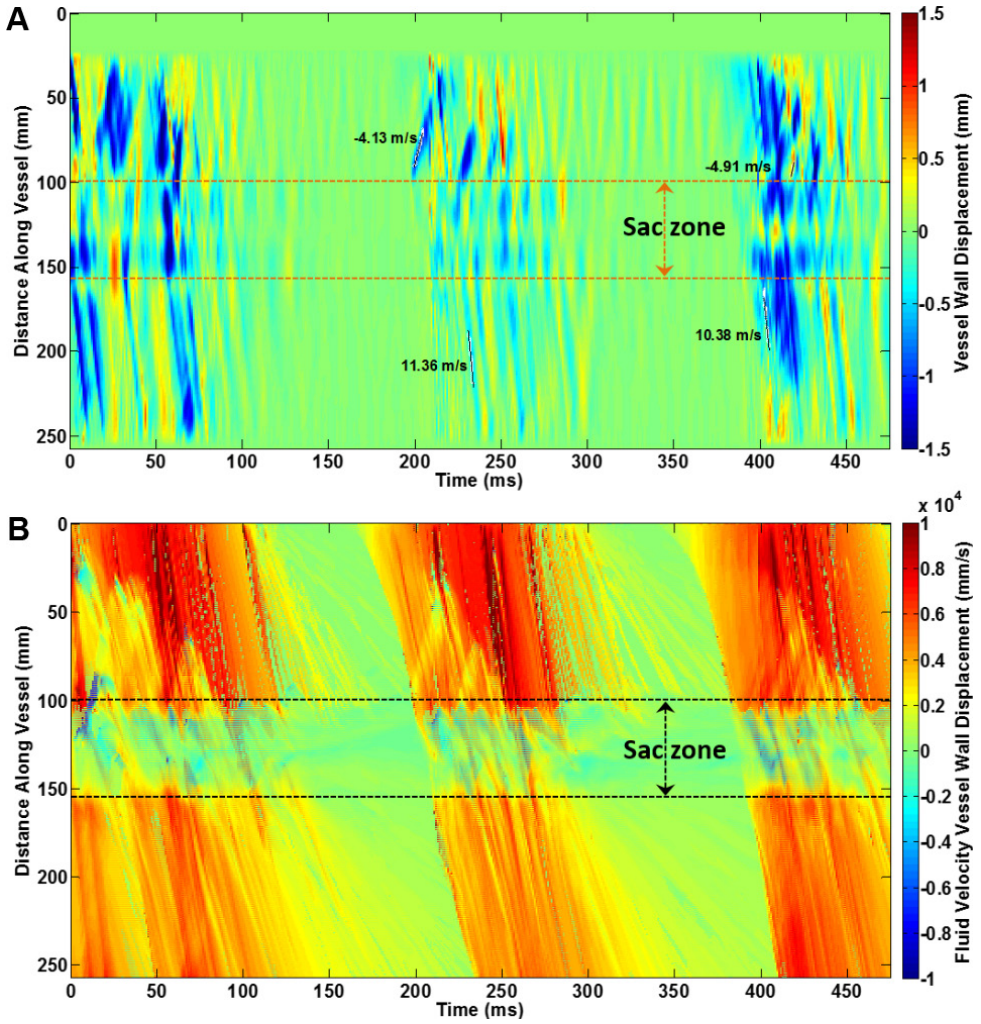

Figure 8. Spatiotemporal maps from the aneurysm geometry aorta with the sac walls 3 times stiffer than the rest of the walls of the aorta. (**A**) Vertical component of the wall displacement. (**B**) Axial component of the fluid velocity.

were performed on the second and third pulse cycles. Most studies on FSI modeling of aneurysmal blood vessels have focused on characterizing parameters such as wall shear stress and pressure in order to find the maximum values and the locations at which they take place.[50,51,54–56] The present study aimed at characterizing the pulse wave propagation on aortas with various material and geometrical properties (Figs. 4, 5, 7, and 8) and identifying markers on the propagation patterns that could be used in experimental phantoms and in vivo PWI studies in which the wall's local irregularities are involved. The wall displacement results indicate the presence of the sac in the aneurysmal geometries (Figs. 5A, 7A and 8A) versus non-aneurysmal geometry (Fig. 4A). Furthermore, within the aneurysmal geometries, multiple forward and reflected waves for each inlet flow cycle are observed, which explains the complexity of implementing the PWI method on diseased aortas, as suggested by others. Part of such phenomena can be explained by the presence of the sac that generates disruption in the wave propagation and causes additional reflections within the sac boundaries. For the straight geometry, the theoretical frequencies of natural vibration modes are f_n = 2.84, 5.68, 8.52, …, kHz, which fall well beyond the excitation frequency of f = 5.4 Hz by the inlet flow; and it is expected that the natural frequencies of the aneurysmal geometries would not deviate much from this range. Therefore, the multiple waves on the wall motions observed here were unlikely to be part of the natural modes of vibrations. However, it has been shown that not incorporating the damping effects into the structural material properties—which otherwise exist in viscoelastic behavior—could cause oscillations in the pressure profile,[49] which can also cause wall oscillations and can partly explain the observations seen here. Based on the straight tube geometry and flow conditions, the flow is expected to be well in the turbulent regime (and beyond the physiological regime), and the presence of the geometrical and material irregularities in the AAA model could only add to the chaotic nature of the fluid (and solid) motions, as seen in the spatiotemporal maps in Figures 5, 7, and 8. Overall, it was found that both

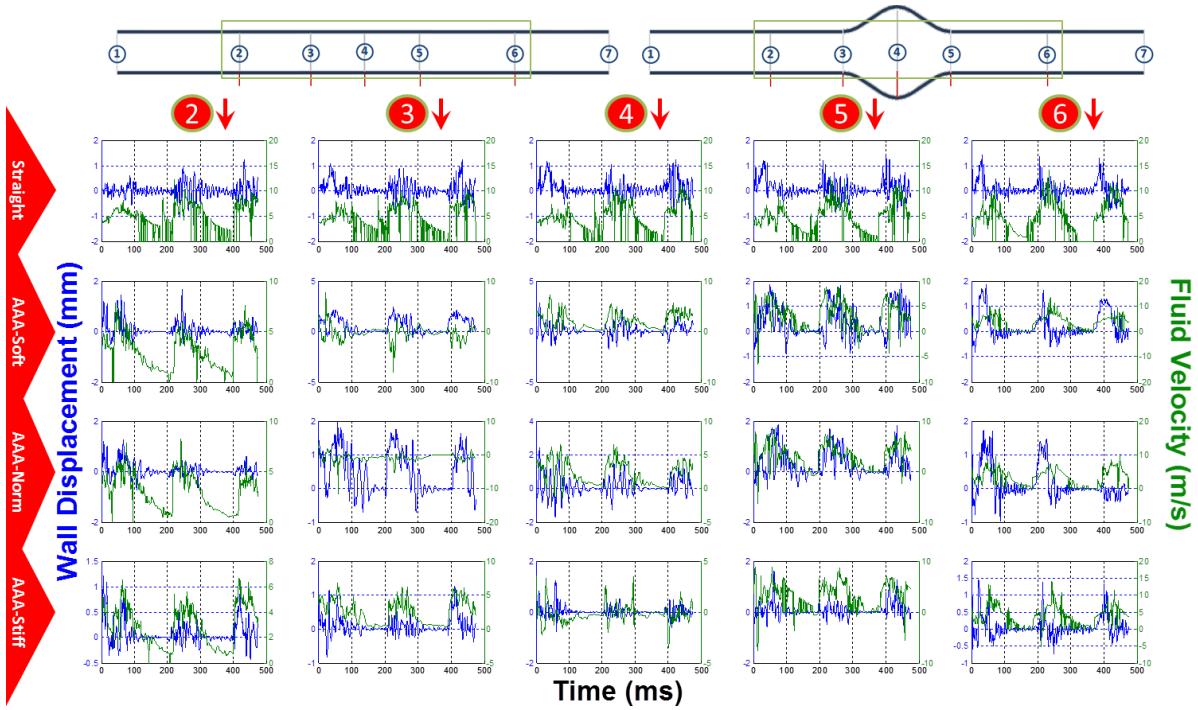

Figure 9. Wall displacement (blue) and fluid velocity (green) for cross sections 2–6 on the straight aorta (first row), AAA aorta with 1.5 time softer sac (second row), for AAA with same stiffness sac (third row), and for AAA with 3 times stiffer sac (fourth row).

the wall displacement and fluid velocity spatiotemporal maps can be used to identify the existence of the sac. However, the wall displacement results were found to be more sensitive to sac stiffness variations. In all AAA-geometry aortas, displacement magnitudes on the sac were found to be higher than the rest of the wall—even for the model with a stiffer sac—perhaps due to a higher pressure gradient inside the sac. Ongoing studies seek to characterize the fluid pressure and the pressure wave propagation as well, in order to gain further insights into how the pressure wave could be related to velocity and displacement waves. Using an average PWV on the forward waves in the straight model to be 10.30 m/s, the dimensions given in Figure 1, and the material properties defined, a Young's modulus of E = 806.18 kPa was obtained using the Moens–Korteweg equation. Although the material was described here as a third-order Ogden model based on the fit to the available experimental data, the low strain range in the same strain–stress curves, ie, ε = 0–2%, yields an average Young's modulus of E = 676.92 ± 36.81 kPa, indicating a 19.09% overestimation of the modulus by the simulation results here. Similar differences between simulation and experimental results have previously been found and explained in detail in terms of the several assumptions underlying each study.[39,40] It should be again noted that the present study was established based on the idealized aneurysm geometry with a simple one-layer aortic wall. Future studies are needed in order to examine the wave dynamics on patient-specific aneurysmal geometries with various diameters of the sac and bifurcations, and with aortic wall composed of intima/media/adventitia layers and thrombus, such as those developed by Lin et al.[64] The accuracy of the results may also be improved by using more physiologically relevant modeling parameters such as material properties and input/boundary conditions. Other studies have shown that modeling the arterial wall as porous,[47] viscoelastic, nonlinear, inhomogeneous,[52] and anisotropic[50] and the fluid as viscous,[55] incompressible, and non-Newtonian[54] affects the FSI dynamics and results in different outputs on the fluid such as shear stress and pressure. More interestingly, in the present study, it was shown that incorporating the viscosity effects into the structural material properties, instead of modeling the structure as purely elastic, helps reduce oscillations in the pulsatile pressure profile[49] and, therefore, in the wall displacement profile. As far as the initial and boundary conditions that were set in this study are concerned, they serve the purpose of simulating the laboratory experimentation of the PWI method, in which a peristaltic device pumps water into an aortic segment that is fully secured on both ends. The full constraint of the tube endings causes artificial stiffening, which affects the wave reflection and dynamics. Improving the initial, boundary, and flow conditions to those relevant to physiological parameters is expected to make the wave dynamics and reflected/forward wave interactions closer to in vivo conditions. Studies are needed to examine such physiologically relevant parameters before any attempts toward clinical implications of simulations results are made.

Conclusion

In this study, dynamic, FSI, finite element simulations have been shown to be promising in modeling the pulsatile flow through arterial models and obtaining the wall displacement and fluid velocity pulse wave propagation. FSI simulations were performed on straight and aneurysmal geometry aortas with softer, the same stiffness, and stiffer sacs, respectively, aiming at examining the effects of geometric and material changes on the pulse wave propagation and velocities. Characterizing such effects can be best performed through simulation studies given that experimental and in vivo specimens with precisely controlled geometry and stiffness might prove costly and/or impossible. The results showed that the presence of the aneurysm sac can be detected through both the wall displacement and fluid velocity propagation profiles observed on the spatiotemporal maps. On average, the within-sac forward waves, pre-sac reflected waves, and post-sac forward waves exhibited orderly, increasing PWVs, all of which also increased with the sac stiffness. The present study is the first report on using numerical models to investigate FSI dynamics of arterial pulsations in aneurysmal aortas. The qualitative and quantitative markers on the wave propagation provided insights that can be used to better guide the experimental and in vivo pulse wave analysis studies.

Acknowledgments

DS would like to thank Dr. Elisa Konofagou and the members of the Ultrasound and Elasticity Imaging Lab (UEIL), Department of Biomedical Engineering, Columbia University, for assisting with the modeling setup and the helpful discussions.

Author Contributions

Conceived and designed the experiments: DS. Analyzed the data: DS, HL, KL. Wrote the first draft of the manuscript: DS. Contributed to the writing of the manuscript: DS, KL, HL. Agree with manuscript results and conclusions: DS. Jointly developed the structure and arguments for the paper: DS. Made critical revisions and approved final version: DS. All authors reviewed and approved of the final manuscript.

REFERENCES

1. Safar ME. Pulse pressure in essential hypertension: clinical and therapeutical implications. *Hypertens*. 1989;7:769–776.
2. Blacher J, Guerin AP, Pannier B, Marchais SJ, Safar ME, London GM. Impact of aortic stiffness on survival in end-stage renal disease. *Circulation*. 1999;99:2434–2439.
3. Laurent S, Boutouyrie P, Asmar R, et al. Aortic stiffness is an independent predictor of all-cause and cardiovascular mortality in hypertensive patients. *Hypertension*. 2001;37:1236–1241.
4. Laurent S, Katsahian S, Fassot C, et al. Aortic stiffness is an independent predictor of fatal stroke in essential hypertension. *Stroke*. 2003;34:1203–1206.
5. Sutton-Tyrrell K, Najjar SS, Boudreau RM, et al. Elevated aortic pulse wave velocity, a marker of arterial stiffness, predicts cardiovascular events in well-functioning older adults. *Circulation*. 2005;111:3384–3390.
6. Laurent S, Cockcroft J, Van Bortel L, et al. Expert consensus document on arterial stiffness: methodological issues and clinical applications. *Eur Heart J*. 2006;27:2588–2605.
7. Mancia G, De Backer G, Dominiczak A, et al. ESH-ESC practice guidelines for the management of arterial hypertension: ESH-ESC task force on the management of arterial hypertension. *J Hypertens*. 2007;25:1751–1762.
8. Bengtsson H, Sonesson B, Bergqvist D. Incidence and prevalence of abdominal aortic aneurysms, estimated by necropsy studies and population screening by ultrasound. *Ann N Y Acad Sci*. 1996;800:1–24.
9. Collins MJ, Eberth JF, Wilson E, Humphrey JD. Acute mechanical effects of elastase on the infrarenal mouse aorta: implications for models of aneurysms. *J Biomech*. 2012;45:660–665.
10. Humphrey JD, Holzapfel GA. Mechanics, mechanobiology, and modeling of human abdominal aorta and aneurysms. *J Biomech*. 2012;45:805–814.
11. Dryjski M, Driscoll JL, Blair RC, et al. The small abdominal aortic aneurysm: the eternal dilemma. *J Cardiovasc Surg*. 1994;35:95–100.
12. Grootenboer N, Bosch JL, Hendriks JM, van Sambeek M. Epidemiology, aetiology, risk of rupture and treatment of abdominal aortic aneurysms: does sex matter? *Eur J Vasc Endovasc Surg*. 2009;38:278–284.
13. Lederle FA, Wilson SE, Johnson GR, et al. Immediate repair compared with surveillance of small abdominal aortic aneurysms. *N Engl J Med*. 2002;346:1437–1444.
14. Darling RC, Messina CR, Brewster DC, Ottinger LW. Autopsy study of unoperated abdominal aortic aneurysms. *Circulation*. 1977;56:161–164.
15. Hall AJ, Busse EFG, McCarville DJ, Burgess JJ. Aortic wall tension as a predictive factor for abdominal aortic aneurysm rupture: improving the selection of patients for abdominal aortic aneurysm repair. *Ann Vasc Surg*. 2000;14:152–157.
16. Vorp DA. Biomechanics of abdominal aortic aneurysm. *J Biomech*. 2007;40:1887–1902.
17. Carmo M, Colombo L, Bruno A, et al. Alteration of elastin, collagen and their cross-links in abdominal aortic aneurysms. *Eur J Vasc Endovasc Surg*. 2002;23:543–549.
18. Dobrin PB. Pathophysiology and pathogenesis of aortic aneurysms. *Surg Clin North Am*. 1989;69:687–703.
19. Nichols W, O'Rourke M. *McDonald's Blood Flow in Arteries: Theoretical, Experimental and Clinical Principles*. 5th ed. London: Hodder Arnold Publication; 2005.
20. Ch C, Nevo E, Fetics B, et al. Estimation of central aortic pressure waveform by mathematical transformation of radial tonometry pressure. Validation of generalized transfer function. *Circulation*. 1997;95:1827–1836.
21. O'Rourke MF, Staessen JA, Vlachopoulos C, Duprez D, Plante GE. Clinical applications of arterial stiffness; definitions and reference values. *Am J Hypertens*. 2002;15:426–444.
22. Fung YC. *Biomechanics: Circulation*. 2nd ed. New York, NY: Springer-Verlag; 1997.
23. Kinsler LE, Frey AR, Coppens AB, Sanders JV. *Fundamentals of Acoustics*. New York, NY: Wiley; 2000.
24. Olufsen MS. Structured tree outflow condition for blood flow in larger systemic arteries. *Am J Physiol*. 1999;276:H257–H268.
25. Pannier BM, Avolio AP, Hoeks A, Mancia G, Takazawa K. Methods and devices for measuring arterial compliance in humans. *Am J Hypertens*. 2002;15:743–753.
26. Lantelme P, Mestre C, Lievre M, Gressard A, Milon H. Heart rate: an important cofounder of pulse wave velocity assessment. *Hypertension*. 2002;39:1083–1087.
27. Millasseau SC, Stewart AD, Patel SJ, Redwood SR, Chowienczyk PJ. Evaluation of carotid-femoral pulse wave velocity: influence of timing algorithm and heart rate. *Hypertension*. 2005;45:222–226.
28. Segers P, Kips J, Trachet B, et al. Limitations and pitfalls of non-invasive measurement of arterial pressure wave reflections and pulse wave velocity. *Artery Res*. 2009;3:79–88.
29. Luo J, Konofagou EE. A fast normalized cross-correlation method for motion estimation. *IEEE Trans Ultrason Ferroelectr Freq Control*. 2010;57:1347–1357.
30. Vappou J, Luo J, Konofagou EE. Pulse wave imaging for noninvasive and quantitative measurement of arterial stiffness in vivo. *Am J Hypertens*. 2010;23:393–398.
31. Westenberg JJ, De Roos A, Grotenhuis HB, et al. Improved aortic pulse wave velocity assessment from multislice two-directional in-plane velocity-encoded magnetic resonance imaging. *J Magn Reson Imaging*. 2010;32:1086–1094.
32. Fujikura K, Luo J, Gamarnik V, et al. A novel noninvasive technique for pulse-wave imaging and characterization of clinically-significant vascular mechanical properties in vivo. *Ultrason Imaging*. 2007;29:137–154.
33. Luo J, Fujikura K, Tyrie LS, Tilson MD, Konofagou EE. Pulse wave imaging of normal and aneurysmal abdominal aortas in vivo. *IEEE Trans Med Imaging*. 2009;28:477–486.
34. Luo J, Lee W-N, Wang S, Konofagou EE. Pulse wave imaging of human abdominal aortas in vivo. *Proc of IEEE Ultrason Symp*. 2008;2008:859–862.
35. Wang S, Lee W-N, Provost J, Luo J, Konofagou EE. A composite high-frame-rate system for clinical cardiovascular imaging. *IEEE Trans Ultrason Ferroelectr Freq Control*. 2008;55:2221–2233.
36. Luo J, Li RX, Konofagou EE. Pulse wave imaging of the human carotid artery: an in vivo feasibility study. *IEEE Trans Ultrason Ferroelectr Freq Control*. 2012;59:174–181.

37. Li RX, Shahmirzadi D, Qaqish WW, Konofagou EE. Performance assessment and optimization of Pulse Wave Imaging (PWI) and its applications for pulse wave analysis in ex vivo canine aortas and in vivo normal human arteries. *Conf Proc IEEE Eng Med Biol Soc*. 2012;2012:3179–3182.
38. Li RX, Luo J, Balaram SK, Chaudhry FA, Shahmirzadi D, Konofagou EE. Pulse wave imaging in normal, hypertensive and aneurysmal human aortas in vivo: a feasibility study. *Phys Med Biol*. 2013;58:4549–4562.
39. Shahmirzadi D, Narayanan P, Li RX, Qaqish WW, Konofagou EE. Mapping the longitudinal wall stiffness heterogeneities within intact canine aortas using Pulse Wave Imaging (PWI) ex vivo. *J Biomech*. 2013;46:1866–1874.
40. Shahmirzadi D, Li RX, Konofagou EE. Pulse-wave propagation in straight-geometry vessels for stiffness estimation: theory, simulations, phantoms and in vitro findings. *J Biomech Eng*. 2012;134:114502.1–6.
41. Shahmirzadi D, Konofagou EE. Detection of aortic wall inclusions using regional pulse wave propagation and velocity in silico. *Artery Res*. 2012;6(3):114–123.
42. Shahmirzadi D, Konofagou EE. Quantification of arterial wall inhomogeneity size, distribution, and modulus contrast using FSI numerical pulse wave propagation. *Artery Res*. 2014;8:57–65.
43. Vappou J, Zervantonakis I, Luo J, Konofagou EE. *Finite Element Modeling of the Pulse Wave propagation in the Aorta for Simulation of the Pulse Wave Imaging (PWI) Method*. New York, NY: Computational Biomechanics for Medicine (MICCAI 2008 Workshop); 2008.
44. Verbeke F, Vanholder R, Rensma PL, et al. Role of aortic calcification, stiffness and wave reflections in cardiovascular risk in dialysis patients: baseline data from the CORD study. *Artery Res*. 2010;4:81–90.
45. Simon BR, Kaufmann MV, McAfee MA, Baldwin AL. Finite element models for arterial wall mechanics. *J Biomech Eng*. 1993;115:489–496.
46. Scotti CM, Jimenez J, Muluk SC, Finol EA. Wall stress and flow dynamics in abdominal aortic aneurysms: finite element analysis vs. fluid-structure interaction. *Comput Methods Biomech Biomed Engin*. 2008;11:301–322.
47. Ayyalasomayajula A, Vande Geest JP, Simon BR. Porohyperelastic finite element modeling of abdominal aortic aneurysms. *J Biomech Eng*. 2010;132(10):104502.
48. Ivankovic A, Karac A, Dendrinos E, Parker K. Towards early diagnosis of atherosclerosis: the finite volume method for fluid-structure interaction. *Biorheology*. 2002;39:401–407.
49. Leung JH, Wright AR, Cheshire N, et al. Fluid structure interaction of patient specific abdominal aortic aneurysms: a comparison with solid stress models. *Biomed Eng Online*. 2006;5:1–15.
50. Rissland P, Alemu Y, Einav S, Ricotta J, Bluestein D. Abdominal aortic aneurysm risk of rupture: patient-specific FSI simulations using anisotropic model. *J Biomech Eng*. 2009;131:31001.
51. Kelly SC, O'Rourke MJ. A two-system, single-analysis, fluid-structure interaction technique for modelling abdominal aortic aneurysms. *Proc Inst Mech Eng H*. 2010;224:955–969.
52. Pelerin JL, Kulik C, Goksu C, Coatrieux JL, Rochette M. Fluid/structure interaction applied to the simulation of Abdominal Aortic Aneurysms. *Conf Proc IEEE Eng Med Biol Soc*. 2006;1:1754–1757.
53. Khanafer K, Berguer R. Fluid–structure interaction analysis of turbulent pulsatile flow within a layered aortic wall as related to aortic dissection. *J Biomech*. 2009;42:2642–2648.
54. Qin J, Zhang J, Chui C-K, et al. A simulation framework for estimating wall stress distribution of abdominal aortic aneurysm. In: 33rd Annual International Conference of the IEEE Engineering in Medicine and Biology Conference; Boston, MA; 2011.
55. Wang X, Li X. Computational simulation of aortic aneurysm using FSI method: influence of blood viscosity on aneurismal dynamic behaviors. *Comput Biol Med*. 2011;41:812–821.
56. Xenos M, Alemu Y, Zamfir D, et al. The effect of angulation in abdominal aortic aneurysms: fluid-structure interaction simulations of idealized geometries. *Med Biol Eng Comput*. 2010;48:1175–1190.
57. Craiem D, Rojo FJ, Atienza JM, Armentano RL, Guinea GV. Fractional-order viscoelasticity applied to describe uniaxial stress relaxation of human arteries. *Phys Med Biol*. 2008;53:4543–4554.
58. Masson I, Boutouyrie P, Laurent S, Humphrey JD, Zidi M. Characterization of arterial wall mechanical behavior and stresses from human clinical data. *Biomechanics*. 2008;41:2618–2627.
59. Laheij R, van Marrewijk C. *Progress Report on the Procedural and Follow Up Results of 3413 Patients Who Received Stent Graft Treatment for Infrarenal Aortic Aneurysms for a Period of 6 Years*. Eindhoven: EUROSTAR Data Registry Centre; 2001.
60. Choke E, Cockerill G, Wilson RW, Sayed S, Dawson J, Loftus IM. A review of biological factors implicated in abdominal aortic aneurysm rupture. *Eur J Vasc Endovasc Surg*. 2005;30:227–244.
61. Fillinger MF, Raghavan ML, Marra SP, Cronenwett JL, Kennedy FE. In vivo analysis of mechanical wall stress and abdominal aortic aneurysm rupture risk. *J Vasc Surg*. 2002;36:589–597.
62. He CM, Roach MR. The composition and mechanical properties of abdominal aortic aneurysms. *J Vasc Surg*. 1994;20:6–13.
63. Xiong J, Wang SM, Zhou W, Wu JG. Measurement and analysis of ultimate mechanical properties, stress-strain curve fit, and elastic modulus formula of human abdominal aortic aneurysm and nonaneurysmal abdominal aorta. *Vasc Surg*. 2008;48:189–195.
64. Lin K, Li H, Shahmirzadi D. Human aortic atherosclerotic plaque characterization under acoustic radiation force impulse using fluid-structural-interface simulations. *Int J Biomed Eng Technol*. 2016.

Appendix

Lagrangian and Eulerian coordinate systems. In the present study, motions of the particles in fluid (ie, flow) and in solid (ie, arterial wall) domains are formulated using Eulerian and Lagrangian coordinate system descriptions, respectively. The implementation of the Eulerian and Lagrangian computations were done here using the CEL solver in Abaqus.

Defining the initial position of a moving particle in the material at the reference time t_0 as $\vec{X}$, the new position of the same particle at the current time t can be obtained as

$$\vec{x} = \vec{\mathbf{X}}(\vec{X}, t) \tag{A1}$$

where $\vec{\mathbf{X}}$ denotes the coordinate transfer function (Fig. A1). Considering the motion of this particle in the Lagrangian coordinate system (eg, such as for the motion of the wall material), the displacement $\vec{U}$, velocity $\vec{V}$, and acceleration $\vec{A}$ of the particle are defined as follows:

$$\begin{aligned} \vec{U}(\vec{X}, t) &= \vec{x} - \vec{X} = \vec{\mathbf{X}}(\vec{X}, t) - \vec{X}; \\ \vec{V}(\vec{X}, t) &= \frac{\partial \vec{U}(\vec{X}, t)}{\partial t} = \frac{\partial \vec{\mathbf{X}}(\vec{X}, t)}{\partial t}; \\ \vec{A}(\vec{X}, t) &= \frac{\partial^2 \vec{U}(\vec{X}, t)}{\partial t^2} = \frac{\partial^2 \vec{\mathbf{X}}(\vec{X}, t)}{\partial t^2} \end{aligned} \tag{A2}$$

The same motion of the same particle can also be described in the Eulerian coordinate system (eg, such as for the motion of the fluid material), in which case the displacement

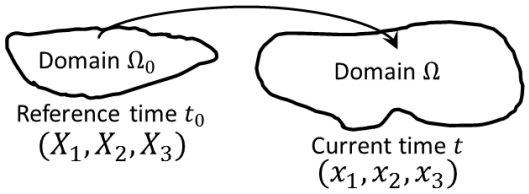

Figure A1. Illustration of particle kinematics between the reference domain Ω_0 and the current domain Ω.

$\vec{u}$, velocity $\vec{v}$, and acceleration $\vec{a}$ of the particle can be defined as follows:

$$\begin{aligned} \vec{u}(\vec{x}, t) &= \vec{x} - \vec{X} = \vec{x} - \vec{\mathbf{X}}^{-1}(\vec{x}, t); \\ \vec{v}(\vec{x}, t) &= \vec{V}\left(\vec{\mathbf{X}}^{-1}(\vec{x}, t), t\right) = \frac{\partial \vec{\mathbf{X}}\left(\vec{\mathbf{X}}^{-1}(\vec{x}, t), t\right)}{\partial t}; \\ \vec{a}(\vec{x}, t) &= \vec{A}\left(\vec{\mathbf{X}}^{-1}(\vec{x}, t), t\right) = \frac{\partial^2 \vec{\mathbf{X}}\left(\vec{\mathbf{X}}^{-1}(\vec{x}, t), t\right)}{\partial t^2} \end{aligned} \tag{A3}$$

Based on the principle of coordinate invariance, the displacement, velocity and acceleration fields obtained from either coordinate system are equal. In finite-element formulations, the Lagrangian mesh topology can be used to describe the solid domains in which the elements are fixed to and move with the particles during the material deformation. Fluid domains, however, can be generated with Eulerian mesh topology, where the elements are fixed in space while the material is allowed to cross in to/out of the element boundaries.